Available online at www.sciencedirect.com
SCIENCE DIRECT®
Computers and Geotechnics 32 (2005) 17–26
COMPUTERS AND GEOTECHNICS
www.elsevier.com/locate/compgeo

Finite element analysis of pile installation using large-slip frictional contact

Daichao Sheng [a,*], K. Dieter Eigenbrod [b], Peter Wriggers [c]

[a] School of Engineering, The University of Newcastle, NSW 2308, Australia
[b] Department of Civil Engineering, Lakehead University, Thunder Bay, Ont., Canada
[c] Institut fuer Baumechanik und Numerische Mechanikt, University of Hannover, Germany

Received 11 May 2004; received in revised form 8 October 2004; accepted 14 October 2004
Available online 15 December 2004

Abstract

This paper presents some observations on stress and displacement characteristics during the installation and loading of pushed-in piles. A commercial finite element code with the capability of simulating large-strain frictional contact between two or more solid bodies is used to simulate the pile installation and pile loading. The soil is treated as a modified Cam clay material, whereas the pile is treated as a rigid body. The computed total resistance and shaft resistance during pile installation are first compared with measured values from centrifuge tests, which indicates that the total resistance is well predicted by the finite element model, but not the shaft resistance. The difference between the computed shaft resistances and the measured values is mainly due to the cone effects introduced in the finite element model. The computed stress paths indicate that both the mean and deviator stresses first increase when the pile cone is above or at the level of the observation point in the soil, and then decreases once the pile cone has moved below the observation point. When the soil is represented by the modified Cam clay model, a thin layer of soil of one pile radius immediately around the pile, extending from the ground surface to a distance of one pile radius above the pile cone, is under elasto-plastic expansion. Just outside this expansion (softening) zone, a compression zone of a 'U' form is observed. The characteristics of the stress paths and volumetric behaviour are not significantly affected by the initial OCR of the soil. The volumetric behaviour is however strongly affected by the constitutive model used for the soil. The so-called h/R effect is also well captured by the finite element model.

Keywords: Pile; Installation; Contact mechanics; Plasticity

1. Introduction

As pointed out by White [11], the behaviour of piles remains one of the largest sources of uncertainty in geotechnical engineering, even though a tremendous amount of research work has been carried out. Much of the uncertainty is due to the lack of understanding of the physical mechanisms that control the characteristics of deformation, strains and stresses in the soil during pile installation and loading. Experimental studies either at model scale or at field scale have led to a wide variety of observations of deformation patterns, stress distributions in soils and pile capacity equations. Some researchers have also turned to numerical modelling for searching for better understanding of pile behaviour under specific, well-defined, but sometimes hypothetical conditions (e.g. [5,7–10]). The apparent advantage of numerical modelling is the completeness of the available information. For example, complete sets of stress and strain fields and pile capacities as well as their sensitivity to various soil and pile parameters can be obtained. Such a numerical approach can indeed lead to some insights of pile behaviour, even though at current stage it can provide only limited input to engineering practice of pile foundations.

* Corresponding author. Fax: +61 2 49216991.
E-mail address: daichao.sheng@newcastle.edu.au (D. Sheng).

0266-352X/$ - see front matter.
doi:10.1016/j.compgeo.2004.10.004

One of the major difficulties in numerical modelling of piles is the modelling of the true installation procedure of the pile or the pile group. In all the cases, the pile or the pile group is placed in a pre-bored hole in the soil and only a small displacement is applied. The obvious shortcoming of this approach is that the effect of the stress changes due to pile installation is not clear.

In this paper, an alternative numerical approach is used to model the installation and loading of single axial piles. The pile–soil interaction is simulated by large-deformation frictional contact between two solid bodies. The contact problem is solved using a Lagrangian multiplier method. With this contact capability, it is possible to simulate the entire installation procedure of a driven pile, namely from the ground surface to a desired depth. The commercial finite element code ABAQUS [1] is used to obtain all the results in this paper, so that interested readers can reproduce the analysis.

2. Finite element model

The pile–soil interaction during pile installation and pile loading is modelled by contact kinematics (see Fig. 1). Updated-Lagrangian finite element formulation is used to model the large-displacement problem. Contact conditions between two surfaces are governed by kinematic constraints in the normal and tangential directions. The normal stress at contact is either zero when there is a gap between the pile and the soil, or compressive when the pile is in contact with the soil. This constraint can be described as

$$\begin{aligned} &\sigma = 0 \quad \text{when } g > 0, \\ &\sigma > 0 \quad \text{when } g = 0, \\ &g\sigma = 0, \end{aligned} \tag{1}$$

where g is the gap, and σ is the normal stress at contact and compression is taken positive. The gap g is never negative because interpenetration of materials is not allowed.

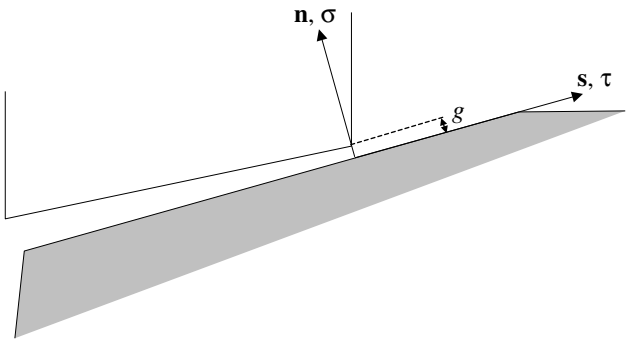

Fig. 1. Contact constraints at soil–pile interface.

The frictional sliding at the pile–soil interface is modelled by the Coulomb friction contact law, i.e. the maximum shear stress at the interface is proportional to the normal stress at the interface. When the shear stress is less than this maximum, no relative displacements (sliding) take place. When the shear stress reaches the maximum, sliding takes place in the direction of the shear stress. The tangential contact conditions can be expressed as

$$\begin{aligned} &u_t = 0 \quad \text{when } \left|\tfrac{\tau}{\mu\sigma}\right| < 1, \\ &u_t > 0 \quad \text{when } \left|\tfrac{\tau}{\mu\sigma}\right| = 1, \\ &\left|\tfrac{\tau}{\mu\sigma}\right| \leqslant 1, \end{aligned} \tag{2}$$

where τ is the tangential stress at contact, μ is the coefficient of friction of the interface, u_t is the relative sliding at contact.

These contact constraints are incorporated into the minimisation of the total potential energy using a Lagrangian multiplier method. For a known assumed set of active contacts, the constrained minimisation problem can be transferred into a set of nonlinear equations in terms of nodal displacements and contact tractions (or Lagrangian multipliers), which are then linearised and solved by the Newton–Raphson iteration. At the start of each Newton–Raphson iteration, a contact search algorithm is used to find the active set of contact constraints according to the current displacement field. Detailed information about finite element simulation and algorithms for frictional contact can be found in text books such as Wriggers [12] as well as in the ABAQUS Theory Manual.

Note that the contact constraints can also be solved by other methods like the penalty method and the augmented Lagrangian method. The penalty method formulates the problem entirely in terms of displacements and only satisfies the contact constraints (1) approximately, depending on a predefined penalty parameter. A larger penalty parameter results in better approximation of contact constraints, but may also lead to ill-conditioning of the global stiffness matrix. The Lagrangian multiplier method, on the other hand, satisfies the contact constraints exactly, but introduces extra degrees of freedom (Lagrangian multipliers) at contact nodes. Its convergence is also often challenging. The augmented Lagrangian method is a combination of a penalty method and a Lagrangian multiplier method and thus enjoys the advantages of the two. These methods as well as other methods are discussed in detail in Wriggers [12]. In the software ABAQUS, only the Lagrangian multiplier method is implemented.

Because the elastic modulus of the steel pile is usually much larger than that of the surrounding soil, the pile is considered as a rigid body for simplicity in this study. Test runs also indicate that the strains in the pile are negligible when the ratio of Young's modulus of the pile

to the shear modulus of the soil is larger than 1000. The soil is modelled as rate-independent elasto-plastic material.

Typical finite element meshes are shown in Fig. 2. The axi-symmetry about the central line of the pile is assumed, which also eliminates the need of a failure or break criterion for the soil. The pile is initially hung above the soil. The soil is discretised into four-noded axi-symmetric quadrilateral elements biased towards the pile. The radial dimensions of the soil elements below and near the pile are typically one-half to one-fourth of the pile's radius.

Due to the strong nonlinearities caused by frictional contact, large deformation and elasto-plasticity, one of the main challenges in this type of numerical analysis is the convergence to a stable solution. The load steps used in the analysis are usually very small. On the other hand, the element size should not be too small. For example, test runs indicate that the optimal size of the soil elements below the pile is about one-half to one pile element, in order to obtain convergent solution without introducing too much mesh error. In addition, test runs also indicate that it is not possible to push a pile with a flat end into the soil in the finite element analysis. Therefore, the conical pile end is chosen with cone angle of 60°, as shown in Fig. 2. The effects of using such a cone instead of a flat end will be discussed in a following section.

In all the analyses in this study, the gravity load is first applied to the soil to establish the initial in situ stress states prior to the pile installation. Such initial stresses are controlled by the given soil unit weights and lateral stress coefficients, K_0. The pile is then pushed into the soil to the desired depth by prescribed displacement. As the soil is modelled as rate-independent material, the velocity of pile driving is not of concern in the analysis. The total resistance acting on the pile is taken as the vertical component of the total force due to contact pressure and frictional stress at the interface, while the shaft resistance of the pile is taken as the vertical component of the total force due to the frictional stress at the interface.

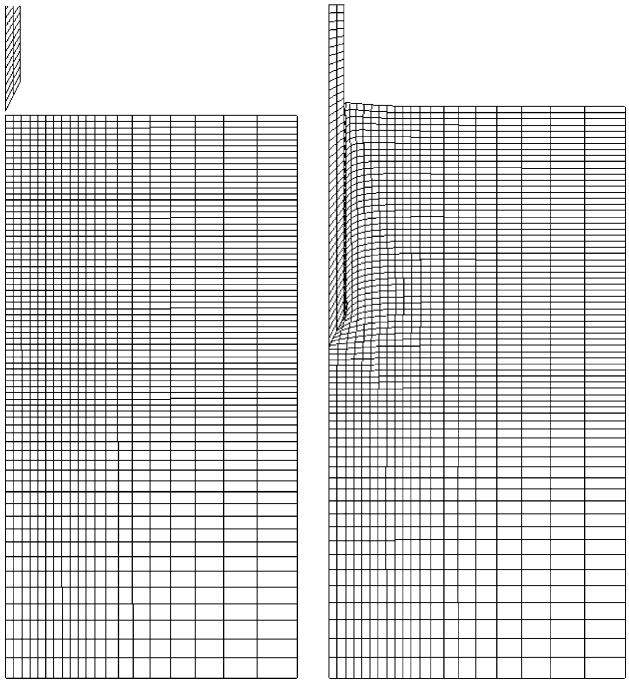

Fig. 2. Typical initial (left) and deformed mesh (right).

3. Axial pile load tests in centrifuge

Hanke [6] conducted a series of centrifuge tests on pressed-in steel piles in dry sand. The sand is a fine silica sand, with an effective grain size $d_{10} = 0.18$ mm, a mean grain size $d_{50} = 0.32$ mm, a uniformity coefficient $C_u = 2.06$, and a specific gravity $G = 2.65$. The sand used in the centrifuge tests was compacted to an average relative density of 76%. The diameters of the piles range between 30 and 40 mm. The pile lengths in the sand range between 225 and 300 mm. The accelerated gravitations range between $50g$ and $66.7g$, with $g = 9.81$ m/s^2.

The geometry and boundary conditions of the finite element simulation of the pile centrifuge tests are shown in Fig. 3. One of Hanke's tests, i.e. Pile 1B2, is simulated in this study. In this test, a pile with a diameter of 30 mm is installed to a depth of 230 mm, at an accelerated gravitation of $66.7g$. In the finite element analysis, the pile end is conical with a cone angle of 60°, as shown in Fig. 3.

A series of triaxial tests on the silica sand were conducted [2] and it was found that its behaviour can be represented relatively well by the modified Cam clay model. The properties listed in Table 1 are derived from these triaxial tests. The friction angle for the steel–sand interface given in Table 1 is obtained by Hanke [6] using standard direct shear tests.

The initial lateral stress coefficient K_0 is assumed to 0.5 for the medium dense sand. The Poisson ratio μ for the sand is assumed to be 0.2. Test runs using μ ranging between 0.1 and 0.4 indicate that this parameter does not significantly affect the total or shaft resistance (see Fig. 4).

4. Cone effects

In theory, the effects of using a cone instead of a flat end for the pile can be studied by varying the angle of the cone. However, when the cone angle is larger than 90°, the pile cannot be pressed into the soil in the numerical analysis using ABAQUS, due to numerical convergence and mesh distortion. Nevertheless, it is hoped

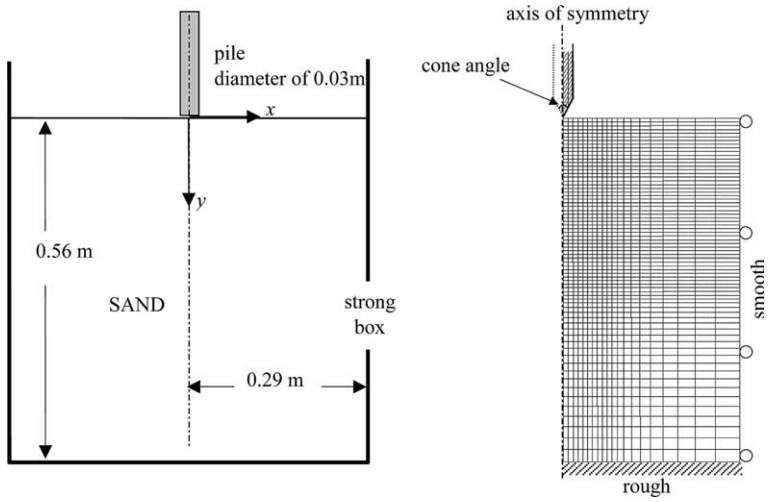

Fig. 3. Geometry, mesh and boundary conditions for the centrifuge test.

Table 1
Soil properties used in the finite element analysis

Soil properties	Value	Units
Gravity acceleration, g	667	m/s^2
Unit weight, γ	15	kN/m^3
Friction angle, ϕ'	33	degree
Initial OCR	4.5	
Slope of normal compression line, λ	0.06	
Slope of unloading–reloading line, κ	0.006	
Poisson's ratio, μ	0.2	
Steel–sand interface friction angle, ϕ_{ps}	27	degree
Lateral stress coefficient, K_0	0.5	
Initial void ratio, e_0	0.96	

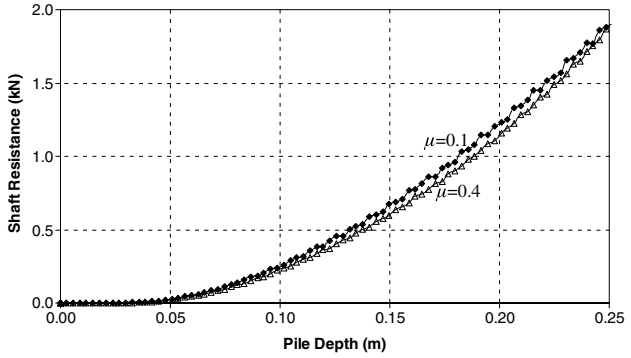

Fig. 4. Effect of the Poisson ratio of the soil.

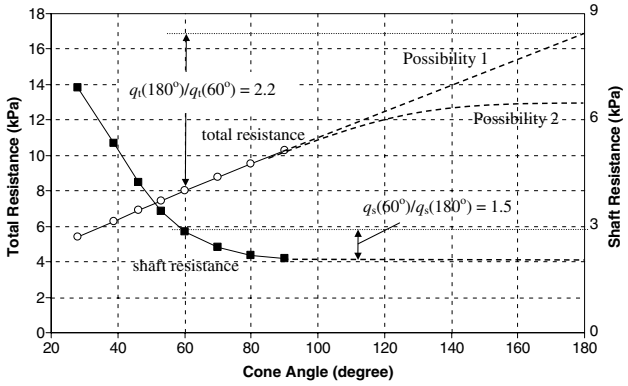

Fig. 5. Effects of the cone angle on the pile resistances.

that the true results for a cone angle of 180° (flat end) can be somehow extrapolated from the results obtained using cone angles less than 90°. To verify this assumption, the pile in Fig. 3, with different cone angles, is pressed into the sand to a depth of 0.24 m. In Fig. 5, the computed total and shaft resistances for the pile are plotted against the cone angle. For the cone angle between 25° and 90°, the total resistance increases linearly with the cone angle, while the shaft resistance decreases gradually to a constant value as the cone angle increases. The tendency of variation of the shaft resistance with the cone angle is reasonably clear for the angles between 90° and 180°. However, the tendency of change of the total resistance with the cone angle between 90° and 180° is not certain. As shown in the figure, there are two possibilities, one is that the total resistance continues to increase linearly with the cone angle, and the other is that it approaches a constant value at certain cone angle. Which pattern will prevail depends, among others, on the ratio of the pile depth to the pile diameter (H/D). For a small H/D, it is reasonable to assume that the total resistance continues to increase with the cone angle [4], whereas for deep piles the total resistance is more likely to be less dependent on the cone angle. Note that in the second possibility it is not certain when the total resistance approaches a constant value. In this study, the depth to diameter ratio H/D is only about 8 and, therefore, even though there is no guarantee that these patterns will continue for cone angles larger than 90°, we assume that the total resistance can be linearly extrapolated from the results obtained

with cone angles less than 90°. In particular, it will be shown in the next section that the extrapolated total resistance agrees well with measured values.

As the numerical analysis for cone angles less than 60° requires very small time steps and becomes difficult, most of the results in this paper are obtained using a cone angle of 60°. While certain results like pile resistances can be corrected to fit flat-ended piles using extrapolation, the effects of the cone on other data like stresses and strains cannot be easily identified. Therefore, all the results presented in this paper, except total resistance and shaft resistance, do not include the effects of the cone angle. While we cannot be certain about the cone effects, it is believed that the same patterns of volumetric strain, stress path, and deformation apply for flat-ended piles.

5. Shaft and end-bearing resistance during pile driving

The computed pile resistances are compared with the measured values from the centrifuge test for Pile 1B2 in Fig. 6. The total pile resistances are taken as the vertical component of the total reaction force on the pile, while the shaft resistances are taken as the vertical component of the total force due to the frictional stress at the soil–pile interface. The total resistances so obtained are then multiplied by a factor of 2.2, to account for the cone effect between a cone angle of 60° used in the model and a cone angle of 180° for the test pile (see Fig. 5). The pile depth is measured from the half height of the cone. It can be seen that the corrected total resistances, which include end-bearing and shaft resistance, compare very well with the measured values, with the former being marginally smaller at small depths. In the centrifuge test, the pile was also unloaded to zero axial load at the depth of 0.19 m. The reloaded total resistance was slightly below the value before the unloading. The recorded final total resistance is 17 kN at depth of 0.23 m. The numerical prediction of the final total resistance at the same depth is 18.5 kN, representing an overestimation of 5%.

The computed shaft resistances in Fig. 6 have been divided by a factor of 1.5, to account for the cone effect (see Fig. 5). The predicted shaft resistances do not agree with the measured values as well as the total resistances. The computed shaft resistances are larger than the measured values by a maximum factor of 3 at the depth of 0.15 m. The predicted final shaft resistance at 0.23 m is 1.6 kN, compared to the measured value of 1.8 kN. It should be noted that the measured shaft resistance is actually the difference between the measured pile load at the top and the tip load at the base. For the flat-ended pile, the shaft resistance is thus expected to be small as the lateral contact pressure with the pile shaft surface is small at small depths. For a conical pile, the contact pressure between the soil and pile develops immediately after the contact has occurred. Therefore, the computed shaft resistances are larger than the measured values at low depths.

6. Deformation and strains

The deformed mesh around the pile is shown in Fig. 7. The soil near most of the pile depth is pushed sidewards and downwards, whereas elements near the top surface are also pushed upwards. In the radial direction, the width of the first column of elements near the pile has been significantly reduced, but the third column of elements is only slightly compressed. This means that most of the radial (sidewards) compression in the soil occurs

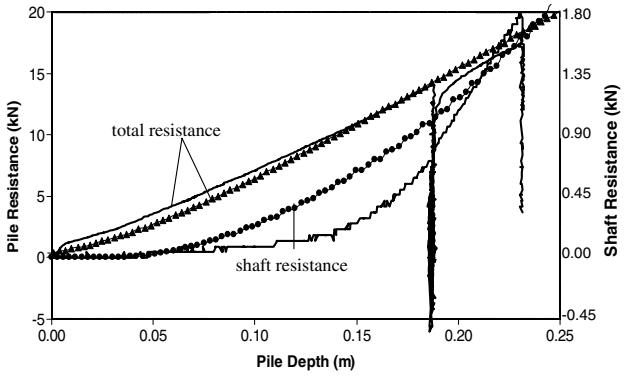

Fig. 6. Measured (solid lines) and computed (dotted lines) pile resistances during installation.

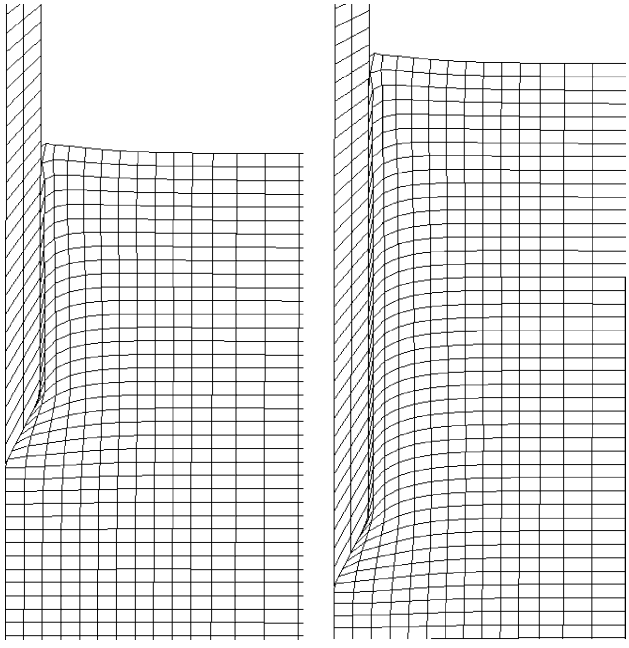

Fig. 7. Deformed mesh during pile installation (left: pile depth 0.144 m; right: 0.24 m).

within a horizontal distance of one pile radius. In the vertical direction, the elements directly below the pile tip are clearly compressed, whereas the elements above the level of the cone base are not significantly compressed. Except a couple of rows of elements near the top surface, the thicknesses of most rows of elements above the level of the cone remain relatively constant, even though the elements near the pile have been sheared downwards. This pattern of deformation suggests that the soil becomes unloaded vertically once the cone has moved below the respective level. It can also be noted that the soil elements below and around the pile are not particularly badly distorted, although deformation and sliding at the soil–pile interface are very large.

The contours of the plastic and total volumetric strains are shown in Fig. 8. It can be seen that a thin zone of soil around the top part of the pile is under plastic expansion (softening). As the pile penetrates deeper, this softening zone expands downwards. Just outside the thin softening zone and beneath the pile, the soil is under plastic compression (hardening). This hardening zone also expands downwards as the pile penetrates deeper. The plastic compression zone is largest at the depth of the cone and then gradually decreases towards the soil surface, but does not reach the surface. The total volumetric strain contours exhibit similar features, with a larger compression zone. It should also be noted that the total volumetric strain contains a small portion of compressive strain from the gravity loading which was applied to establish the initial stress state. This is why the total volumetric strain is not zero away from the pile. Realising that the zero total volumetric strain in Fig. 8 actually means expansion during pile installation, we also notice that there is an expansion zone developed some distance beneath the pile tip (or just below the compression zone).

Test runs also indicate that the deformation pattern is not significantly affected by the initial OCR of the soil, though it does depend on the constitutive model used for the soil. This type of behaviour is further discussed in the stress path study.

7. Stresses and stress path

The computed stress contours for the pile depth of 0.24 m are shown in Fig. 9. The radial stress (S11) has a maximum value of about 8400 kPa near the pile cone. This is compared to the initial radial stress of 120 kPa at the depth of 0.24 m. The stress concentration bulb extends to a radius roughly $10R$, with R being the pile radius. Beneath the pile tip, the radial stress decreases rapidly from high compressive stress to zero at a distance of about $5R$. The vertical stress (S22) has a maximum value of 6000 kPa just beneath the cone, compared to the initial value of 240 kPa at 0.24 m. Compared to the radial stress bulb, the vertical stress bulb is smaller in the radial direction ($\sim 6R$), but larger in the vertical direction ($\sim 10R$). The vertical stress does not exhibit a zero zone beneath the pile tip. However, there is a small zone above the cone where the vertical stress is in tension. Note that the mean stress in this zone is still in compression as the constitutive model requires.

The circumferential stress (S33) experiences the smallest increases amongst the three normal stresses. The maximum circumferential stress is about 4800 kPa, again just beneath the cone. However, the stress concentration bulb has extended to the boundary in the radial direction. In addition, there is a thin band around the pile (about $9R$ distance away from the pile) where the circumferential stress is in tension. The shear stress (S12) displays a usual 'X' form, with the crossing point located at the cone. The maximum shear stress is around 3600 kPa, again just beneath the cone.

The stress paths at four observation points are shown in Fig. 10, where the effective mean stress in compression is positive. Because of the large-stress range, both the mean stress and the deviator stress are plotted in logarithmic values. In such a double log plot, the K_0 line and the critical state line (CSL) are parallel. All four observation points are initially located at $x = 0.002$ m, i.e. almost at the centre line. It can be seen that the four stress paths follow the same pattern, but end at different positions depending on the relative distance to the cone tip. We can thus take the stress path at point ($x = 0.002$, $y = 0.125$) as an example. The stress path is characterised by four phases. It first follows an initial elastic path (AB) where the effective mean stress decreases slightly and the deviator stress increases. The stress path AB corresponds to the initial elastic compression of the soil below the pile tip. Point B is located on the softening part of the yield surface or the so-called dry side of the CSL. However, further penetration of the pile does not cause any softening or expansion of the soil, but causes the stress path to follow the current yield surface, also called 'neutral loading'. Along the stress path BC, the soil at the observation point is further compressed as the pile is approaching its level, but is not yet in contact with the pile tip. Point C is located on the hardening part of the yield surface or the wet side of the CSL. From point C on, the stress path follows very closely (but stays below) the CSL till Point D. Plastic compression (hardening) takes place during the path CD and both the mean and deviator stresses increase significantly. Point D corresponds to the position where the shoulder of the pile (cone/cylinder transition) is just at the level of the observation point in the soil. Once the cone has moved below this level, the mean and deviator stresses decrease, following the CSL, however, slightly above. From Fig. 8, it can be noticed that the soil expands once it moves above the pile shoulder. Therefore, plastic softening, not elastic unloading, occurs along the stress path DE.

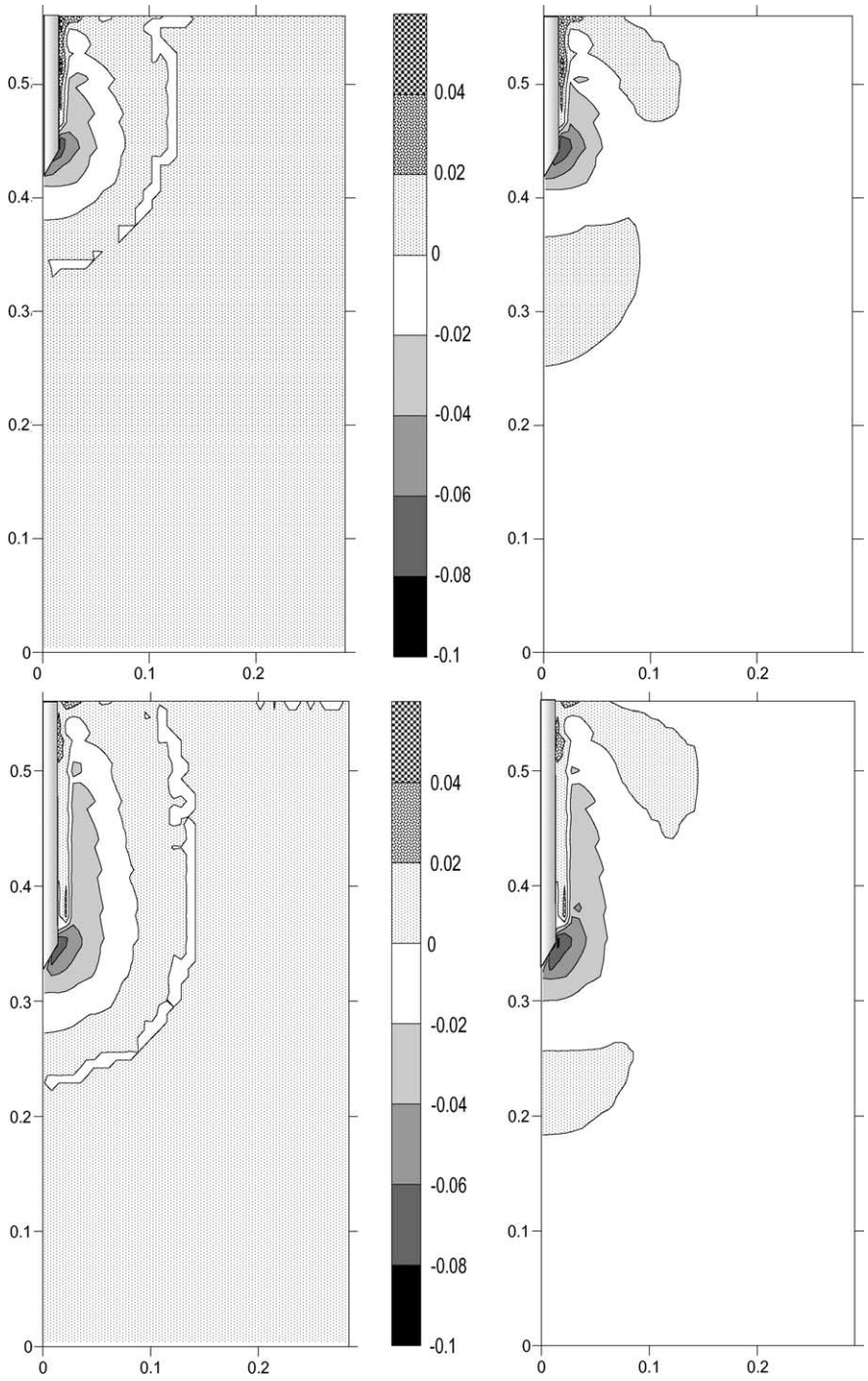

Fig. 8. Volumetric strain developed during pile installation (left: plastic volumetric strain; right: total volumetric strain; top: depth 0.144 m; bottom: 0.24 m; expansion: positive).

The stress paths at 1 or 2 radius away from the pile axis are very similar to those shown in Fig. 10, except ending at different stages along ABCDE, depending on their distances to the pile tip and the pile axis. The characteristics of the stress paths observed here are rather similar to those observed by Chow (1997, cited in [11]) in field tests. Test runs using smaller and larger OCR values indicate that the general pattern of the stress path is not significantly influenced by the OCR. With an OCR less than 2, the deviator stress at point B would be very close to but below the critical state line. This type of stress path behaviour conforms with the OCR-independent volumetric behaviour observed before.

It should also be noted that the stress paths are less influenced by the constitutive model than the strain

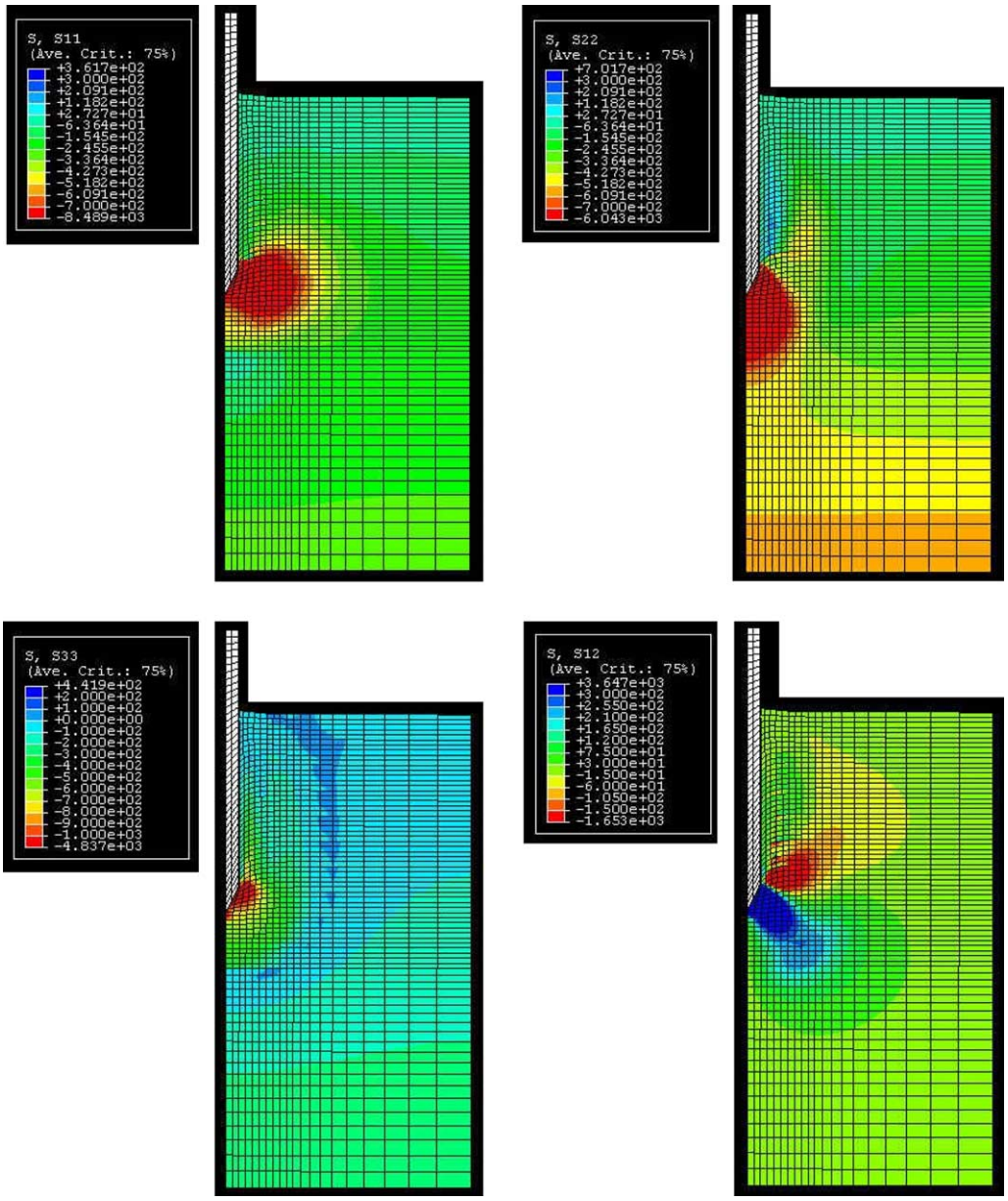

Fig. 9. Stress contours at the end of pile installation (S11: radial stress; S22: vertical stress; S33: circumferential stress; S12: shear stress; unit: kPa).

paths. For example, if a Mohr–Coulomb model were used for the soil behaviour, the stress paths would exhibit the same pattern, except that the points B, C, D and E would then follow the Mohr–Coulomb failure line. However, the volumetric strain behaviour would be quite different from that shown in Fig. 8, because the Mohr–Coulomb model is not able to simulate plastic volume compression.

8. Friction fatigue – the *h*/*R* effect

It was observed that the radial stress and thus also the shaft friction experience a sharp decrease behind the pile tip. This feature is referred to as 'friction fatigue' by Heerema (1980), or as the '*h*/*R* effect' by Bond and Jardine [3]. From the stress path diagram Fig. 10, we have already seen the sharp decrease of the mean and deviator stresses once the pile cone has passed the observation point in the soil. In Fig. 11, the radial stresses for three different *h*/*R* ratios are plotted against depth and compared with the initial radial stresses, with *h* being the depth of the pile tip and *R* being the pile radius. All the curves display a sharp increase in the radial stress just above the cone and a zone of small radial stress (smaller than the initial K_0 radial stress) at some distances below the cone tip.

For $h/R = 4.0$, the radial stress increases from about 10 kPa to about 400 kPa over a depth of 0.006 m. The radial stress remains very high along the length of the

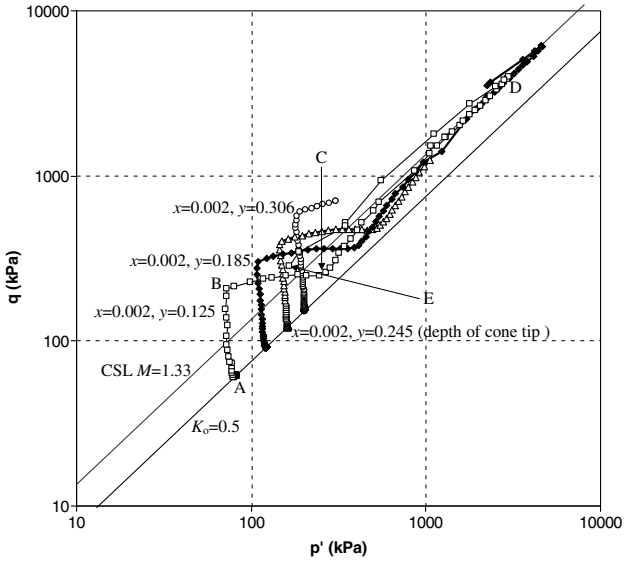

Fig. 10. Stress paths during pile installation (the x and y values are initial coordinates before the pile was installed, see Fig. 3).

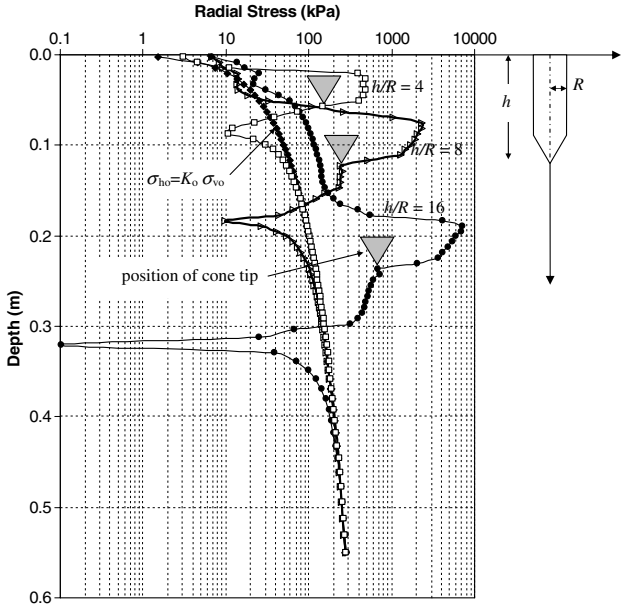

Fig. 11. Profile of radial stresses at $x = 0.002$ (compression positive).

cone, but decreases sharply from the cone tip to the depth of 0.09 m (about one pile diameter below the cone tip). Its value at the depth of 0.09 m is only one-fourth of the initial K_0 radial stress. The radial stress gradually recovers to the initial K_0 value at the depth 0.15 m (about two pile diameters below the cone tip).

For $h/R = 8$, the radial stress at the depth of 0.04 m (about one pile diameter above the cone) is actually smaller than the initial K_0 radial stress. It increases from about 14 kPa at 0.04 m to about 2000 kPa at 0.08 m (about half a pile diameter above the cone). Again, the radial stress remains relatively high along the cone length, and then drops dramatically at the cone tip to about 200 kPa. It remains relatively constant for a depth of about one pile diameter below the cone tip, and then further drops to a minimum of 10 kPa at the depth of 0.18 m (about two pile diameters below the cone tip). The minimum radial stress below the cone tip is much less than the initial K_0 stress, indicating an unloading in the radial direction. The radial stress recovers to the K_0 value at the depth of about 4–5 pile diameters below the cone tip.

The curve for $h/R = 16$ basically follows the same pattern as that for $h/R = 8$, except having a larger stress increase just above the cone (to a maximum of 7000 kPa) and a larger stress decrease below the cone tip (to a minimum of 0.1 kPa). In general, the results in Fig. 11 indicate that, as the pile tip moves closer to and passes an observation point in the soil, the soil is first unloaded in the radial direction, then loaded to a high compressive radial stress and then unloaded again. The unloading in the radial stress when the pile tip has passed the observation point also corresponds to the stress path DE in Fig. 10. Therefore, the so-called h R effect, which is well captured in the numerical results here, is associated with the softening of the soil around the pile and above the cone.

9. Conclusions

Installation and loading of axial pushed-in piles are modelled using large-slip frictional contact between solid bodies. Some stress and displacement characteristics during the installation and loading of displacement piles are presented. A commercial finite element code with the capability of simulating large-deformation and frictional contact is used to carry out the simulation. It has been shown that it is possible to model the entire installation process of a pushed-in pile, using contact kinematic constraints. However, due to the difficulties in convergence in the numerical analysis, some special care and even modification must be taken. One of them is that a conic pile end must be used instead of a flat end.

The computed total resistance and shaft resistance during pile installation are first compared with measured values from centrifuge tests, which indicates that the total resistance is well predicted by the finite element model, but not the shaft resistance. The difference between the computed shaft resistances and the measured values is mainly due to the cone effects introduced in the finite element model. The computed stress paths indicate that both the mean and deviator stresses first increase when the pile cone is above or at the level of the observation point in the soil, and then decreases once the pile cone has moved below the observation point. When the soil is represented by the modified Cam clay model, a thin soil layer of one pile radius immediately around the pile, extending from the ground surface to a distance

of one pile radius above the pile cone, is under elasto-plastic expansion. Just outside this expansion (softening) zone, a compression zone of a 'U' form is observed. The characteristics of the stress paths and volumetric behaviour are not significantly affected by the initial OCR of the soil. The volumetric behaviour is however strongly affected by the constitutive model used for the soil. The so-called h/R effect is also well captured by the finite element model.

This paper presents an alternative method for modelling pile behaviour. The promising part is that the pile installation process can be modelled. However, more research is required on robust and accurate numerical algorithms for solving contact problems before more realistic and complex features like piles with flat ends, piles under cyclic compression and tension, piles installed by hammering, and piles in fine-grained soils with excess pore pressure development, can be considered.

References

[1] ABAQUS/Standard User's Manual, Version 6.2, Hibbitt, Karlsson & Sorensen; 2001.

[2] Birn L. Influence of pile embedment length to diameter ratio on the shaft resistance of pipe piles subjected to axial load reversals. M.Sc. Thesis, Faculty of Engineering and Applied Science, Memorial University of Newfoundland: Canada; 2004.

[3] Bond AJ, Jardine RJ. Effects of installing displacement piles in a high OCR clay. Geotechnique 1991;41(3):341–63.

[4] Durgunoglu HT, Mitchell JK. Static penetration resistance of soils. In: Proceedings of the conference on in situ measurement of soil properties. ASCE J Geotech Eng, vol. 1;1975: 151–89.

[5] De Nicola A, Randolph MF. Tensile and compressive shaft capacity of piles in sand. ASCE J Geotech Eng 1993;119(12): 1952–73.

[6] Hanke R. Shaft capacities of closed end pile under load reversals in sand. MSc Thesis, Memorial University of Newfoundland: Canada; 2001.

[7] Lee JH, Salgado R. Determination of pile base resistance in sands. ASCE J Geotech Geoenviron Eng 1999;125(8):673–83.

[8] Mabsout ME, Reese LC, Tassoulas JL. Study of pile driving by finite element method. ASCE J Geotech Eng 1995;121(7):535–43.

[9] Poulos HG. Pile behaviour – theory and application. Geotechnique 1989;39(3):360–415.

[10] Sagaseta C, Whittle AJ. Prediction of ground movements due to pile driving in clay. ASCE J Geotech Geoenviron Eng 2001;127(1):55–66.

[11] White DJ. An investigation into the behaviour of pressed-in piles. PhD dissertation, University of Cambridge; 2002.

[12] Wriggers P. Computational contact mechanics. New York: Wiley; 2002.